ChemComm

COMMUNICATION

Check for updates

In situ integration of bimetallic NiFe Prussian blue analogs on carbon cloth for the oxygen evolution reaction†

Zhiyong Wang,‡[ad] Shusheng Wan,‡[b] Yuanmao Chen,[ad] Juntao Ren,*[e] Lin Liu,[c] Panpan Yuan,[c] Qiong Luo,[c] Peng Deng,[c] Zheng Liang, [ID][ad] Xinyang Yue*[ad] and Junxiong Wang*[ad]

This study develops a cost-effective strategy to integrate the bimetal NiFe Prussian blue analog (PBA) on carbon cloth (NFPB@CC) as a highly-active oxygen evolution reaction (OER) hybrid catalyst. NFPB@CC possesses abundant unsaturated metal active sites, with a low OER overpotential of only 332 mV and a low Tafel slope of 78 mV dec^{-1} at 10 mA cm^{-1}.

Hydrogen is one of the most promising power sources to tackle environmental concerns due to its sustainable and pollution-free nature.[1] Electrochemical water-splitting consists of two half-reaction processes.[2] The oxygen evolution reaction (OER), a four-electron process, requires a higher oxidation overpotential than hydrogen evolution (HER) to overcome its high reaction kinetic barrier.[3] This greatly limits its efficiency for energy conversion. Therefore, it is critical to search for electroactive materials with high activity and stability as catalysts to speed up the process. Noble metal oxides, such as RuO$_2$ and IrO$_2$, have excellent oxygen evolution capability as benchmark catalysts.[4] However, their high costs and poor durability limit large-scale practical applications.[5]

Although the cheap Prussian blue (PB) has raised great attention, directly utilizing PB as OER catalysts could not obtain optimal electrocatalytic performance due to their poor conductivity and limitations of the coordinatively unsaturated surface atomic sites.[6] In this regard, numerous research efforts have been placed to improve the activity of PB. Specifically, the Prussian blue analogs (PBAs) possess more abundant unsaturated metal active sites and bimetallic coordinative coupling effect for the OER.[7] Zheng and coworkers confirm that the bimetallic Fe-doped Ni-PBA shows faster kinetics and higher conductivity than the monometallic Ni-PBA. It is discovered that doping Fe not only modifies the electronic structure of Ni-PBA, improves its conductivity, and increases the number of active sites, but also enhances electron transfer between the electrode and electrolyte, thereby enhancing electrocatalytic OER activity and durability.

Nonetheless, the electrocatalytic activity and long-term stability of the bimetallic PBA-derived catalysts are still below expectations.[8] One of the possible reasons could be the use of binders to adhere active particles onto conductive substrates, which easily leads to the reduction of the active area and an increase in contact resistance. Obviously, *in situ* synthesis of PBAs on 3D conductive substrates could make the active material bond strongly to the substrate.[9] This can not only improve the mechanical stability of the active materials but also promote electron transfer by excellent connection with the conductive substrate beneath. Carbon cloth (CC) is an excellent substrate whose surface contains abundant functional groups that favor the *in situ* synthesis and growth of PBA nanoparticles.[10] Besides, CC can enhance the conductivity of the catalyst and offer a flexible backbone.[11] However, a facile strategy for *in situ* assembly of NiFe-PBA (NFPB) materials on CC has rarely been reported.

In this work, we report a facile and cost-effective strategy to integrate the bimetallic NFPB on CC (NFPB@CC) to improve the OER performance. The role of the NFPB@CC in regulating the OER process is investigated, and we found that the synergistic effect of Ni/Fe and the high overall conductivity is the key. Moreover, the pores of CC drastically improve the overall kinetics of the catalyst by facilitating bubble desorption and mass transfer. This work paves the way for the exploitation of bimetallic NFPB for large-scale water-splitting applications.

[a] Frontiers Science Center for Transformative Molecules, School of Chemistry and Chemical Engineering, Shanghai Jiao Tong University, Shanghai 200240, China. E-mail: xinyangyue@sjtu.edu.cn, wjx1992@sjtu.edu.cn

[b] School of Mechanical Engineering, Shanghai Jiao Tong University, Shanghai 200240, China

[c] School of Materials Science and Engineering, Jiangxi University of Science and Technology, Ganzhou 341000, China

[d] Zhangjiang Institute for Advanced Study, Shanghai Jiao Tong University, Shanghai, 200240, China

[e] Department of Catalytic Materials, Henan Newmight Company, Xuchang 461700, China. E-mail: hfhgchrjt@163.com

† Electronic supplementary information (ESI) available: Experimental section, photographs of NFPB@CC, SEM images and XPS spectra of the samples, V–t and CV curves, and chronopotentiometry curves. See DOI: https://doi.org/10.1039/d4cc06260d
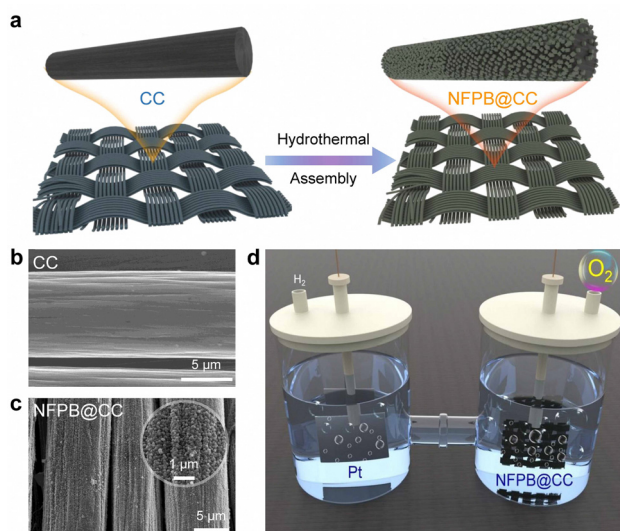
‡ These authors contributed equally to this work.

Fig. 1 (a) Schematics of CC and NFPB@CC. SEM images of (b) the CC fiber and (c) NFPB@CC. (d) Illustration of the electrocatalytic OER process using NFPB@CC as the catalyst.
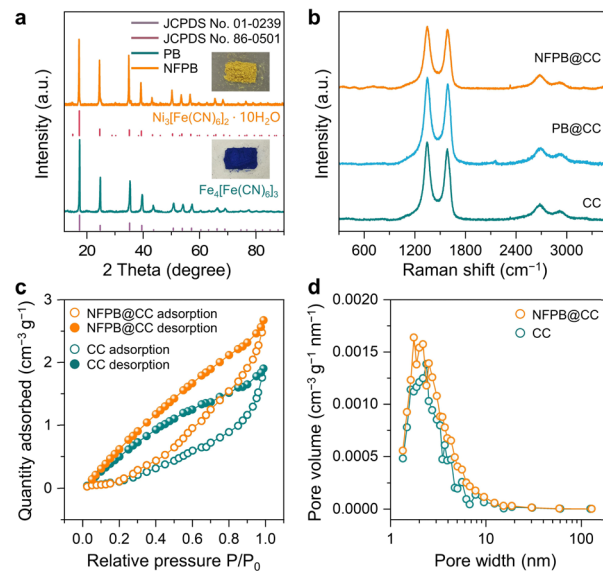

Fig. 2 (a) X-ray diffraction (XRD) patterns of PB and NFPB. (b) Raman spectra of CC, PB@CC, and NFPB@CC. (c) N_2 adsorption/desorption isotherms and (d) pore size dispersion plots of CC and NFPB@CC.

The NFPB@CC was *in situ* synthesized by means of a simple one-step hydrothermal self-assembly method, as shown in Fig. 1a. It needs to be noticed that the purchased pristine CC keeps floating on the water in a beaker due to its hydrophobicity (Fig. S1a, ESI†), which could partially be ascribed to a small amount of impurities on the surface of the pristine CC fiber, as found by SEM (Fig. S2, ESI†). Fig. 1b and Fig. S3a and b (ESI†) show that the impurities could be removed from the surface after concentrated acid soaking. The hydrophilicity of pre-treated CC was significantly enhanced such that the treated CC could be freely settled to the bottom of the beaker (Fig. S1b, ESI†). Hydrophilic CC fibers could be used as ideal substrates for uniform growth of NFPB. Numerous NFPB nano-cubes were distributed uniformly over the CC fibers (Fig. 1c and Fig. S4a, ESI†). *In situ* growth of PBAs particles on conductive carbon fiber substrates without adhesives facilitates exposure of active sites and enhances electron transport.

The synthetic solution of NFPB displays a yellow color after aging, which differed from the dark blue of PB (Fig. S1c and d, ESI†), indicating the different structures of the as-prepared NFPB with PB. It is noteworthy that PVP and sodium citrate dihydrate were added as chelating agents to facilitate slow nucleation and controlled crystal growth of PBAs.[12] Due to poor electrical conductivity of PBAs, the conductivity of the catalyst can be effectively improved with the carbon fibers, and the process of charge transfer is accelerated in the electrochemical OER process (Fig. 1d). The NFPB@CC could be bent at a certain angle, which implied excellent flexibility (Fig. S4b, ESI†).

SEM and TEM images show that there is no significant difference between the PB and NFPB (Fig. S3c and d, ESI†). The particle size of the cubic PB is about 100 nm. While for NFPB, the size is about 150 nm. The characteristic peaks of PB and NFPB match well with the crystal facets of $Fe_4[Fe(CN)_6]_3$

(JCPDS no. 01-0239) and $Ni_3[Fe(CN)_6]_2\cdot10H_2O$ (JCPDS no. 86-0501), respectively (Fig. 2a). The high-resolution TEM (HR-TEM) image (Fig. S5a and b, ESI†) reveals that the distinct lattice fringes with interplanar distance of 0.208 nm could be attributed to the (422) plane of NFPB. The corresponding energy dispersive X-ray spectroscopy (EDS) of NFPB reveals that the contents of Ni, Fe, N, and C are 0.33, 0.23, 0.54 and 82.19, respectively (Fig. S5c, ESI†). It is worth mentioning that the excessive carbon content was attributed to the carbon support film of the TEM's copper wire.

The NFPB@CC was further studied by Raman spectra, as presented in Fig. 2b. The broad Raman bands at 678, 549, and 476 cm^{-1} could be attributed to A_{1g}, T_{2g} and E_g vibration modes of the $NiFe_2O_4$ structure, respectively.[13] The peaks of 2160 cm^{-1} represent Fe^{2+}-CN-Ni^{2+} in NFPB.[14]

Moreover, to examine the porosity and pore size distribution, N_2 sorption experiments were carried out for NFPB@CC and CC. The multi-point BET surface area of NFPB@CC is $\sim2.1\ m^2\ g^{-1}$, which is larger than that of CC ($\sim0.86\ m^2\ g^{-1}$). This enhancement indicates improved active site accessibility. Fig. 2c displays the N_2 adsorption–desorption isotherms of NFPB@CC and CC, which are in accordance with type IV isotherms, suggesting the mesoporous nature. In Fig. 2d, the pore diameter of NFPB@CC is smaller than that of CC. The optimized surface structure promotes O_2 desorption between CC fibers, accelerating the catalytic process.

The surface composition and element states of NFPB@CC and its counterparts were analyzed *via* X-ray photoelectron spectroscopy (XPS). In Fig. 3a, the full survey spectrum for NFPB consists of five elements (C, O, N, Fe, and Ni), confirming Ni incorporation. In contrast, the full spectrum of PB@CC reveals only Fe (Fig. S6a, ESI†). From the C 1s spectrum in Fig. 3b, the fitted peaks at 283.5, 284.8, and 286.5 eV are assigned to metal–C, C–C, and C–N of $[Fe(CN)_6]^{4-}$, respectively.[15] Compared with the O 1s spectrum of PB@CC (Fig. S5c, ESI†),
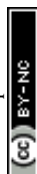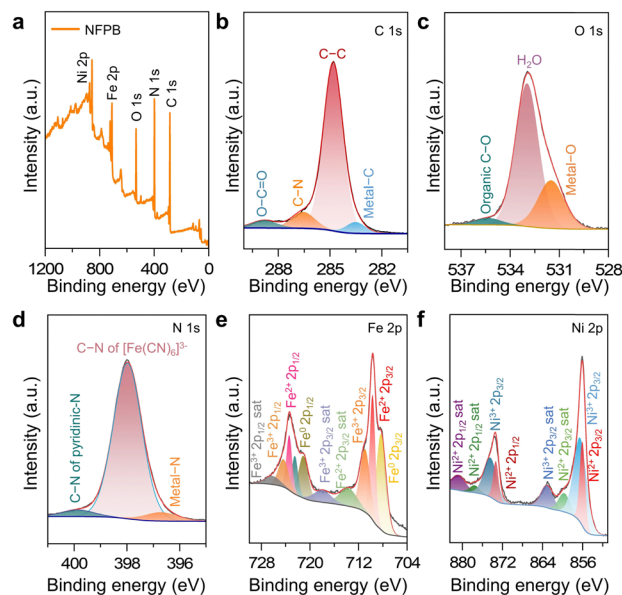
Fig. 3 (a) The XPS full spectrum of NFPB@CC. The XPS spectra of (b) C 1s, (c) O 1s, (d) N 1s, (e) Fe 2p, and (f) Ni 2p for NFPB@CC.
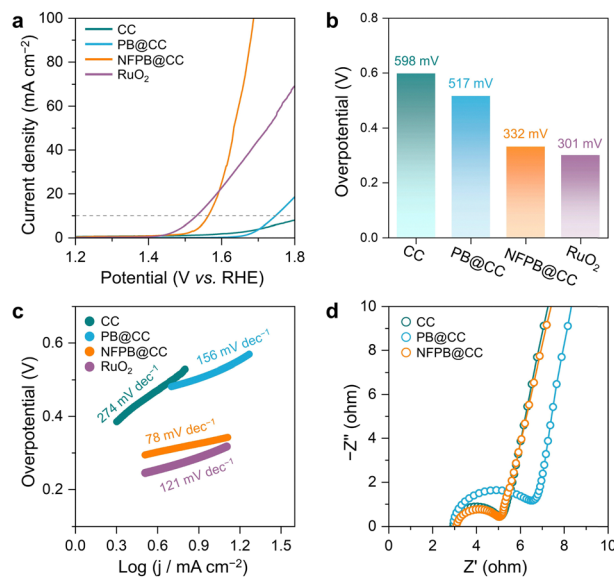

Fig. 4 (a) The OER polarization curves of different samples and (b) the corresponding overpotentials. (c) Tafel profiles and (d) Nyquist plots of different samples in 1 M KOH electrolyte.

NFPB contains the O−H bond of H_2O (Fig. 3c). This corresponds to the formula $Ni_3[Fe(CN)_6]_2 \cdot 10H_2O$ from the XRD test. It suggests that the large void inside the NFPB lattice is filled with certain H_2O molecules.[16] Hence, NFPB@CC may form stronger bonds to H_2O than PB@CC. For the N 1s spectrum of NFPB@CC (Fig. 3d) and PB@CC (Fig. S5d, ESI†), the metal−N binding energy of NFPB@CC (396.6 eV) is higher than that of PB (396.3 eV). This shows that the oxidation number of the N element increases and the electron cloud density decreases after Ni doping.[17] It is beneficial to reduce the repulsive force on H_2O and improve the OER performance.

Furthermore, there are Fe^{2+} and Fe^{3+} states in NFPB@CC (Fig. 3e). This indicates that the Fe element is not only present in $[Fe(CN)_6]^{4-}$, but also a few Fe^{3+} ions occupy the Ma site of $A_xM_a[M_b(CN)_6]^{y-} \cdot nH_2O$.[18] The fitting plots of the Fe 2p spectrum of PB@CC contain eight apparent peaks in Fig. S5e (ESI†). This shows that there are both Fe^{2+} and Fe^{3+} states in PB, which corresponds to the formula "$Fe^{III}_4[Fe^{II}(CN)_6]_3$" of PB. For the Ni 2p spectrum (Fig. 3f), the peaks at 856.0 eV (Ni $2p_{3/2}$) and 873.3 eV (Ni $2p_{1/2}$) can be assigned to Ni^{2+}.[19] For the NFPB catalyst, the electronic structure of the original Fe element of PB changes after doping Ni. The electronic structure of the redistributed catalyst is more favorable to reducing the adsorption energy of the OER reaction intermediates (M–O). In addition, Ni and Fe have a variety of valence states. They can synergistically adsorb OH^-, which makes the catalytic process more efficient.

To evaluate the OER performance, the prepared catalysts were investigated in 1 M KOH electrolyte using a standard three-electrode setup. Before OER measurements, the working electrodes were electrochemically pretreated by repeating cyclic voltammetry (CV) for 20 cycles from 0.812 to 1.012 V (vs. RHE) at 100 mV s^{-1}. For the linear sweep voltammetry (LSV)

polarization curves, we first tested three kinds of NFPB@CC materials synthesized by different Ni/Fe molar ratios (5 : 1, 3 : 1, 1 : 1). This indicated that NFPB31@CC shows lower OER overpotential by comparing experimental data with NFPB51@CC and NFPB11@CC (Fig. S7, ESI†). Hence, NFPB@CC with the Ni/Fe ratio of 3 : 1 was selected to further perform electrochemical measurements. As shown in Fig. 4a, NFPB@CC shows excellent OER activity due to the active NFPB nanocubes and optimal electronic structure between Ni and Fe active sites. NFPB@CC exhibits a lower overpotential of 332 mV at 10 mA cm^{-2} in comparison to bare CC (598 mV) and PB@CC (517 mV) (Fig. 4b), which is similar to conventional RuO_2 (301 mV). When the current density reaches 70 mA cm^{-2}, NFPB@CC exhibits a drastically low overpotential of only 430 mV compared with 590 mV for RuO_2 (Fig. 4a). Furthermore, the large amounts of oxygen bubbles also could be continuously released from the NFPB@CC (1 cm × 1 cm) electrocatalyst at a large current density of 100 mA cm^{-2} (Movie S1, ESI†). This result indicates that NFPB@CC is more suitable for water electrolysis than RuO_2 under the condition of industry-level high current densities.

Tafel slope is another factor to evaluate the catalytic kinetics process of the OER. In Fig. 4c, NFPB@CC displays the lowest Tafel slope of only 78 mV dec^{-1} compared to the RuO_2 benchmark and other samples. Due to the structural coordination relationship between Ni and Fe in NFPB nanoparticles, NFPB@CC possesses abundant coordinative active sites for optimal OER kinetics. Besides, CC greatly promotes the process of interfacial charge transfer for the OER. Fig. 4d depicts the Nyquist plots of NFPB@CC, demonstrating a lower interfacial charge-transfer resistance (R_{ct}) of NFPB@CC. Because of the poor conductivity of PB, the R_{ct} delivered by the PB@CC system increased remarkably. In addition, compared to the reported
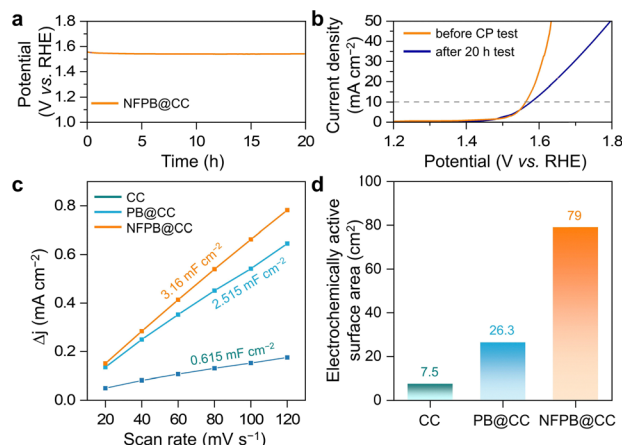
Fig. 5 (a) The CP profile of NFPB@CC at 10 mA cm^{-2} for 20 h. (b) The LSV curve of NFPB@CC before and after the CP test. (c) The Δj plotted against scan rate for different samples. (d) The electrochemically active surface area of different samples.

materials containing Ni or Fe with self-supporting substrate, our NFPB@CC catalyst exhibits superior OER activity (Table S2, ESI†). The long-term stability of the NFPB@CC catalyst is one of the most crucial factors for potential practical application and was evaluated by a chronopotentiometry (CP) test. In Fig. 5a, the voltage curve shows high stability without obvious fluctuations during continuous electrolysis for over 20 h at 10 mA cm^{-2}. After the CP test, the LSV curve of NFPB@CC is basically consistent with the initial test results, which show an 18 mV increase in polarization potential (Fig. 5b) and stable fluctuation over 28 h (Fig. S8, ESI†). CV tests were conducted to investigate the double-layer capacitance (C_{dl}) on NFPB@CC (Fig. S9, ESI†). The peak current densities are linearly correlated with respect to the corresponding scan rates (Fig. 5c).[20] Obviously, the C_{dl} of NFPB@CC (3.16 mF cm^{-2}) is superior to that of CC and PB@CC, leading to a higher electrochemically active surface area (79 cm^2), as shown in Fig. 5d.[6]

In summary, we developed an effective method to *in situ* integrate the bimetallic NFPB on CC. Due to the synergistic effect of Ni and Fe active sites, the electronic structure of the NFPB nanocubes could be regulated to enhance the OER performance when serving as a catalyst. With NFPB stuck strongly with the 3D CC skeleton, the conductivity and electrochemically active area of NFPB@CC were improved dramatically to accelerate the OER kinetic process. As a result, NFPB@CC exhibited excellent OER capability that only required 332 mV and 430 mV overpotential in 1.0 M KOH aqueous solution at 10 and 70 mA cm^{-2}, respectively. NFPB@CC also maintained stability in the two-day electrolysis process for potential long-term application.

Data availability

The data supporting this article have been included as part of the ESI.†

Conflicts of interest

There are no conflicts to declare.

Notes and references

1 H. F. Wang, L. Chen, H. Pang, S. Kaskel and Q. Xu, *Chem. Soc. Rev.*, 2020, **49**, 1414.
2 J. Gautam, Y. Liu, J. Gu, Z. Ma, J. Zha, B. Dahal, L.-N. Zhang, A. N. Chishti, L. Ni, G. Diao and Y. Wei, *Adv. Funct. Mater.*, 2021, **31**, 202106147.
3 A. Saad, D. Liu, Y. Wu, Z. Song, Y. Li, T. Najam, K. Zong, P. Tsiakaras and X. Cai, *Appl. Catal., B*, 2021, **298**, 120529.
4 C. Wei, Z. Wang, K. Otani, D. Hochfilzer, K. Zhang, R. Nielsen, I. Chorkendorff and J. Kibsgaard, *ACS Catal.*, 2023, **13**, 14058.
5 S. Li, S. Zhao, F. Hu, L. Li, J. Ren, L. Jiao, S. Ramakrishna and S. Peng, *Prog. Mater. Sci.*, 2024, **145**, 101294.
6 X. Zhang, I. U. Khan, S. Huo, Y. Zhao, B. Liang, K. Li and H. Wang, *Electrochim. Acta*, 2020, **363**, 137211.
7 Z. Yang, H. Niu, F. Yu, X. Xie, K. Qian, K. Bian, M. Xiang and S. Dong, *J. Colloid Interface Sci.*, 2022, **628**, 588.
8 J. Zhao, J. J. Zhang, Z. Y. Li and X. H. Bu, *Small*, 2020, **16**, 202003916.
9 L. L. Wu, X. H. Chen, Q. Zhang, J. Luo, H. C. Fu, L. Shen, H. Q. Luo and N. B. Li, *Appl. Surf. Sci.*, 2021, **567**, 150835.
10 Z. Wang, J. Ren, G. Ling, J. Guo, Y. Lv and R.-P. Ren, *Adv. Sci.*, 2025, **12**, 2407631.
11 Z. Zhao, K. Xia, Y. Hou, Q. Zhang, Z. Ye and J. Lu, *Chem. Soc. Rev.*, 2021, **50**, 12702.
12 M. Hu, S. Furukawa, R. Ohtani, H. Sukegawa, Y. Nemoto, J. Reboul, S. Kitagawa and Y. Yamauchi, *Angew. Chem., Int. Ed.*, 2012, **51**, 984.
13 A. Ahlawat and V. G. Sathe, *J. Raman Spectrosc.*, 2011, **42**, 1087.
14 W. Zhang, Y. Zhao, V. Malgras, Q. Ji, D. Jiang, R. Qi, K. Ariga, Y. Yamauchi, J. Liu, J.-S. Jiang and M. Hu, *Angew. Chem., Int. Ed.*, 2016, **55**, 8228.
15 S. Lv, H. Luo, Z. Wang, J. Yu, Y. Cheng, F. Chen and X. Li, *Carbon*, 2024, **218**, 118668.
16 J. Li, L. He, J. Jiang, Z. Xu, M. Liu, X. Liu, H. Tong, Z. Liu and D. Qian, *Electrochim. Acta*, 2020, **353**, 136579.
17 Q. Yin, T. Xu, F. Cao, Y. Wang, C. Yang, N. Liu, J. Liu and R. Liu, *Electrochim. Acta*, 2024, **476**, 143749.
18 S. Chong, J. Yang, L. Sun, S. Guo, Y. Liu and H.-K. Liu, *ACS Nano*, 2020, **14**, 9807–9818.
19 M. Du, P. Geng, C. Pei, X. Jiang, Y. Shan, W. Hu, L. Ni and H. Pang, *Angew. Chem., Int. Ed.*, 2022, **61**, e202209350.
20 J.-Y. Gao, Y.-L. Ma, G.-S. Qian, M.-Y. Si, L.-L. Han and J.-S. Li, *Chem. Commun.*, 2024, **60**, 14224–14227.